Dual Charge Transfer Mechanisms in Intimately Bonded S-scheme Heterojunction Photocatalyst with Expeditious Activity towards Environmental Remediation

Potlako J. Mafa[1,], Mope E. Malefane[1] Francis Opoku[2], Adewale O. Oladipo[3], Gcina Mamba[1], Tunde L. Yusuf[4], Jemal Fito Nure[5], Sogolo L. Lebelo[3], Dan Liu[1,6], Jianzhou Gui[1,6], Bhekie B. Mamba[1,6], Alex T. Kuvarega[1]*

[1]*Institute for Nanotechnology and Water Sustainability, College of Science, Engineering and Technology, University of South Africa, Florida Campus, 1709, Johannesburg, South Africa*

[2]*Department of Chemistry, Kwame Nkrumah University of Science and Technology, Kumasi, Ghana*

[3]*Department of Life and Consumer Sciences, College of Agriculture and Environmental Sciences, University of South Africa, Private Bag X06 Florida 1709, Johannesburg, South Africa*

[4]*Department of Chemistry, Faculty of Natural and Agricultural Sciences, University of Pretoria, Hatfield 0028, Pretoria, South Africa*

[5]*School of Chemical and Metallurgical Engineering, University of the Witwatersrand, 1 Jorissen St, Johannesburg, 2000, South Africa*

[6]*State Key Laboratory of Separation Membranes and Membrane Processes, Tianjin Key Laboratory of Green Chemical Technology and Process Engineering, School of Chemistry and Chemical Engineering, Tiangong University, Tianjin 300387, China*

*Corresponding author's email: mafapj@unisa.ac.za; mafa.027@gmail.com

Text S1. Characterization techniques

The surface morphology, structural features, and composition of the samples were analyzed using a Zeiss Auriga FESEM instrument coupled with an EDX spectrometer with an Oxford detector. The internal morphology was analyzed on a JEOL JEM-2100 HRTEM instrument operated at an acceleration voltage of 200 kV. An AutoSorb iQ3 (Quantachrome Instruments) was used for specific surface area and porosity analysis after degassing the samples at 100 °C for 6 h. The purity and crystallinity were assessed using a Rigaku Ultima IV X-ray powder diffractometer (CuKα radiation source, λ = 0.15406 nm). To examine the functional groups present in the catalysts, a PerkinElmer Frontier FTIR spectrometer was used for functional group analysis. An Alpha 300, TS 150 WITec confocal Raman spectrometer at a magnification of 20X and 532 nm laser power was used for bonding vibrations. A TGA 5500 Discovery series (TA instruments) was used for thermal analysis under nitrogen conditions. XPS spectra were recorded on a Thermo ESCAlab 250 Xi spectrometer using an Al Kα (1486.7 eV) monochromatic X-ray radiation source. UV–vis DRS spectra were obtained from a PerkinElmer Lambda 650S spectrometer using $BaSO_4$ as a reference. A Horiba Fluorolog-2 Jobnyvon spectrofluorometer was used for photoluminescence (PL) analysis at an excitation wavelength of 330 nm. The hydrophobicity and hydrophilicity were assessed through contact angle measurements using a DSA30E Kruss drop-shape analyzer.

Text S2. Photoelectrochemical assessment

The photoelectrochemical properties of the prepared materials were investigated using an Autolab potentiostat workstation (PGSTAT204, Netherlands). The experimental setup consisted of a three-electrode configuration: a platinum wire as the counter electrode (Pt wire), a reference electrode (Ag/AgCl, 3.0 M KCl), and a working electrode (fabricated photoanodes). Before analysis, photoanodes were fabricated as follows: fluorine-doped tin oxide (FTO) was used as a substrate with a geometric area of 1.5 cm by 1.5 cm. The sample was cleaned repeatedly using acetone and deionized water under ultrasonication before drying at 60 °C for 5 min. Then, 50 mg of the photocatalyst, 5 wt% polyvinylidene fluoride (PVDF), and 100 µL of N-methyl-2-pyrrolidone (NMP) were mechanically mixed to form a slurry, which was dispersed uniformly on the FTO surface by the drop-casting method. Subsequently, the photoanodes were dried for 4 h in an oven at 60 °C to ensure solidification and stability. The photoanodes were placed under a xenon solar lamp with a power rating of 100 W as the light source. A solution of 5 mM $[Fe(CN)6]^{3-/4-}$ in 0.1 M KCl was used as a redox couple for the

measurement of impedance spectroscopy with a +0.25 V potential in the frequency range of 100 kHz to 0.1 Hz. The photocurrent measurements were performed by employing chronoamperometry in 0.1 M Na_2SO_4 solution under an on/off light switch.

Text S5. Results and Discussions

The FTIR was performed to confirm the functional groups, identities, and interactions of the materials, as indicated in Figure S1a. The spectra of MBO and dCN display typical IR vibrations at approximately 3404 and 3489–3138 cm^{-1}, which correspond to the O–H and N–H stretching vibrations of uncondensed amino groups, respectively.[1] In MBO, the bands located at 861, 679, 511, and 424 cm^{-1} indicate the vibrations of Bi–O–Bi/Bi=O, Mg–O, and Bi–O, respectively, while the broad peak at 1474–1386 cm^{-1} emanates from the Bi–O–Bi vibration.[2] These results further indicate that the prepared material is α-Bi_2O_3. The IR spectrum of dCN has peaks at approximately 1637–1247 cm^{-1} arising from C–N and C=N moieties in tri-s-triazine, whereas those at 894 and 810 cm^{-1} confirm the presence of N–H bonds and the characteristic identity pattern of tri-s-triazine, manifesting the production of graphitic carbon nitride.[1,3] Coincidental to the Raman spectra of the 1:1, 1:3, and 1:5 composites, new peaks are observed at approximately 627 and 579 cm^{-1} in the spectra of the specified composites; these peaks are linked to the formation of Bi-N bridges.

Thermal stability was assessed in a temperature range of 20 to 800 °C in the air at a rate of 10 °C min^{-1} to evaluate the stability and identity of the materials (Figure S1b). MBO and MBOdCN displayed high thermal stability, with total mass losses of 3.70% and 0.86%, respectively. The dCN displays the typical and unique thermal stability of graphitic carbon nitride, with 5.80% and 94.20% mass loss below 200 °C and 680 °C, respectively, similar to what has been reported in the literature.[1] This was due to the volatilization of moisture, destruction of the periodic graphitic backbone, and complete carbonization of the tris-s-triazine moiety. Surprisingly, the composite material displays the strongest stability, which could mean that the sample is stabilized by the formation of interactive bonds and can be used even at high temperatures for different applications.

In addition, nitrogen adsorption-desorption analysis was carried out to evaluate the BET-specific surface area, porosity, and textural properties of the materials, as shown in Figure S1c. As indicated, the MBO, dCN, and MBOdCN samples display type IV classification with H3 hysteresis loops according to the IUPAC classification, which is indicative of the mesoporous structure of the photocatalyst.[4] The BET-specific surface areas of the MBO, dCN, and

MBOdCN samples were determined to be 8.45, 64.41, and 7.33 m^2 g^{-1}, respectively, with corresponding pore volumes (pore diameters) of 0.10 (2.74), 1.67 (3.42), and 0.07 (3.06) cm^3 g^{-1} (nm), respectively. Notably, the specific surface area of MBOdCN is significantly smaller than that of dCN and slightly smaller than that of MBO, which is evidence of the close hybridization of the two materials to form the composite. Although a reduction in the surface area could mean a reduced number of active sites, the high performance of the composite material could be linked to the effective impedance of charge carriers compounding due to the reduction in the coulombic force.

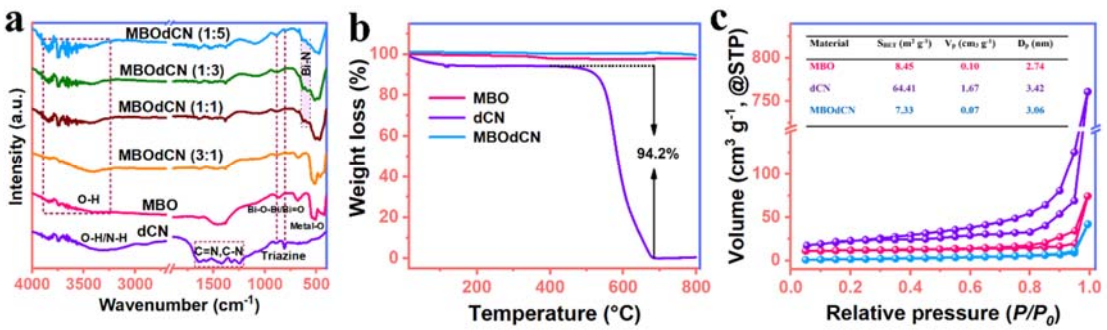

Figure S1. (a) FTIR vibrations, (b) thermal stability, and (c) nitrogen adsorption-desorption isotherms of photocatalysts.

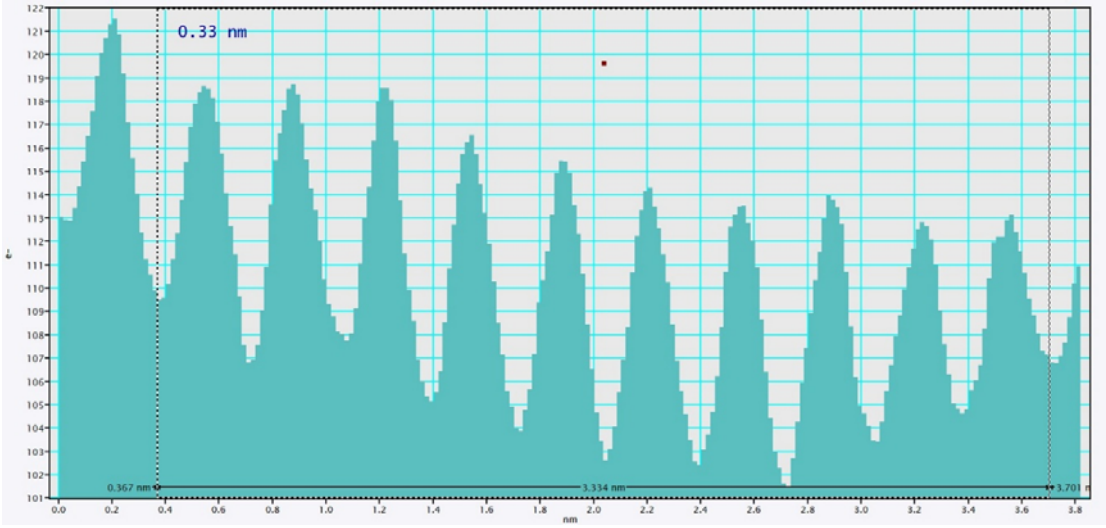

Figure S2. Live profile image of MBOdCN material.

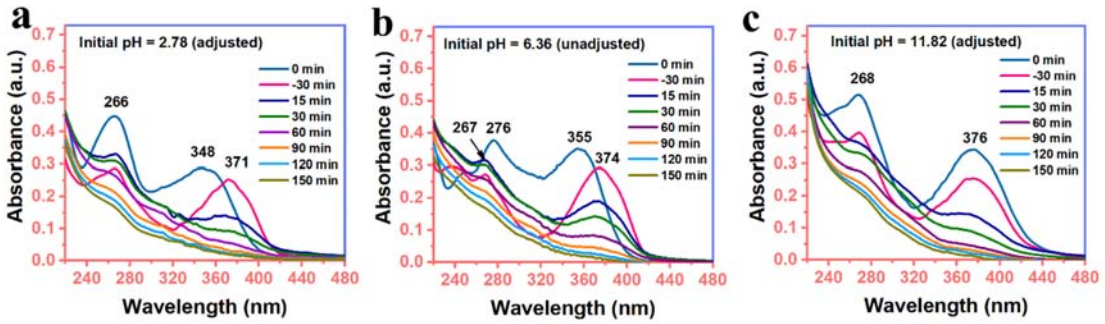

Figure S3. (a-c) Temporal evolution of the visible absorption spectra at different pH values during the photodegradation of OTC under visible light.

The electronic structure was explored to determine the mechanism underlying the enhanced photocatalytic performance of the MBOdCN photocatalyst. The calculated indirect bandgaps of MBO, dCN, and the MBOdCN S-scheme heterostructure are 2.63, 1.64, and 2.14 eV, respectively (Figure S4d-f). This indicated that the HSF06 functional group could validate the individual structures' and heterostructures' experimental bandgap values. As shown in Figure S4d-f, analysis of the total density of states (TDOS) and partial density of states (PDOS) of the MBO, dCN, and MBOdCN from –4 to 4 eV was performed to confirm the contributions of the different orbitals of Bi, O, Mg, C, and N atoms to the material properties. Thus, the PDOS was analyzed to determine the atomic orbital that contributes the most to charge transfer. The calculated PDOS of MBO is shown in Figure S4d. The O-2*p* orbital contributed most to the valence band maximum (VBM). In contrast, the Bi-6*p* orbital had a small but important contribution to VBM. In contrast, the conduction band minimum (CBM) had the most significant contribution from the Bi-6*p* orbital, with a smaller contribution from the O-2*p* orbital, confirming the covalent nature of the material [5]. The calculated PDOS of dCN (Figure S4e) revealed that the majority of the states in both the CBM and VBM are C-2*p* and, to a lesser extent, N-2*p*. After the formation of the MBOdCN heterostructure, the electronic structures of the MBO and dCN were successfully retained, with dCN and MBO dominating the VBM and CBM of the MBOdCN as depicted in Figure S4f. This demonstrated that charge moves from dCN to MBO in the MBOdCN heterostructure, thus taking the form of a type II heterostructure.[6] However, when the photogenerated electrons and holes in the MBOdCN heterojunction separate and transfer through a conventional type II process, there will be less favorable conditions for the formation of $^{\bullet}OH$ and $^{\bullet}O_2^-$ reactive species, which ultimately leads to reduced photoactivity toward pollutant degradation.[7] Hence, the formation of a type II heterojunction was very unlikely to occur in this system. Based on the above discussion and

the results of scavenger tests and XPS, it is clear that the MBOdCN composite follows a typical S-scheme charge transfer mechanism as opposed to the conventional type II system.[8] To account for the enhanced photocatalytic performance of the MBOdCN composite, a plausible S-scheme mechanism involving the separation of electron-hole pairs is proposed and elaborated, as shown in Figures 6 and 7. Concerning the PDOS in Figure S4f, the VBM is largely contributed by the C-2*p* and N-2*p* states, whereas the CBM is dominated primarily by Bi-6*p* and O-2*p* states.

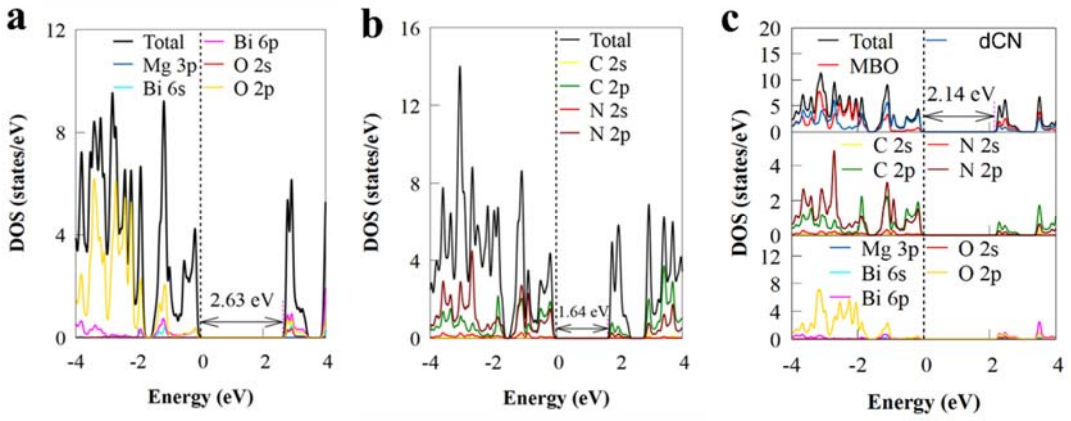

Figure S4. The density of states of (a) MBO, (b) dCN, and (c) the MBOdCN heterostructure. The Fermi level is shown by the black dashed lines with zero energy.

The evaluation of the MBOdCN heterostructure stability was performed considering the binding energy (E_b) as follows: $E_b = (E_{\mathrm{MBOdCN}} - E_{\mathrm{MBO}} - E_{\mathrm{dCN}})/S$, where E_{MBOdCN}, E_{MBO}, E_{dCN}, and S are the energies of the MBOdCN heterostructure, MBO, dCN and interface area, respectively.[9] The obtained E_b of -16.34 meV Å^{-2} is fairly small, and the interlayer distance between MBO and dCN is 3.52 Å. The MBOdCN heterostructure is energetically stable, and the negative value is consistent with an exothermic process. Furthermore, E_b is closer to the vdW binding energy, which ranges from -13 to -20 meV Å^{-2}.[10] The stability of the heterostructure was further confirmed by calculating the phonon spectra and performing *ab initio* molecular dynamics (AIMD) simulations in addition to the E_b. The calculated vibrational phonon spectra are shown in Figure S5a-c as evidence of dynamic stability. As depicted in Figure S5a-b, the phonon dispersion without imaginary frequencies along the Brillouin zone displays dynamic stability in MBO and dCN. The study of the MBOdCN is theoretically supported by these findings, which demonstrate the good kinetic stability of MBO and dCN. Most significantly, the phonon spectrum curve with no virtual frequency highlights that the

MBOdCN possesses kinetic stability. AIMD simulation was used to verify the thermal stability of the MBOdCN photocatalyst. It is evident from Figure S5d that the time-dependent total energy and temperature fluctuations are nearly constant after heating for 25 ps at 1 fs time steps, confirming the high thermal stability of the MBOdCN at ambient temperature (300 K). Collectively, these results strongly support the resilience and structural integrity of the heterostructure, as shown by the stability of the total energy during the simulation and preservation of the original structural framework. After the establishment of structural stability, the electronic behavior of the heterostructure was examined.

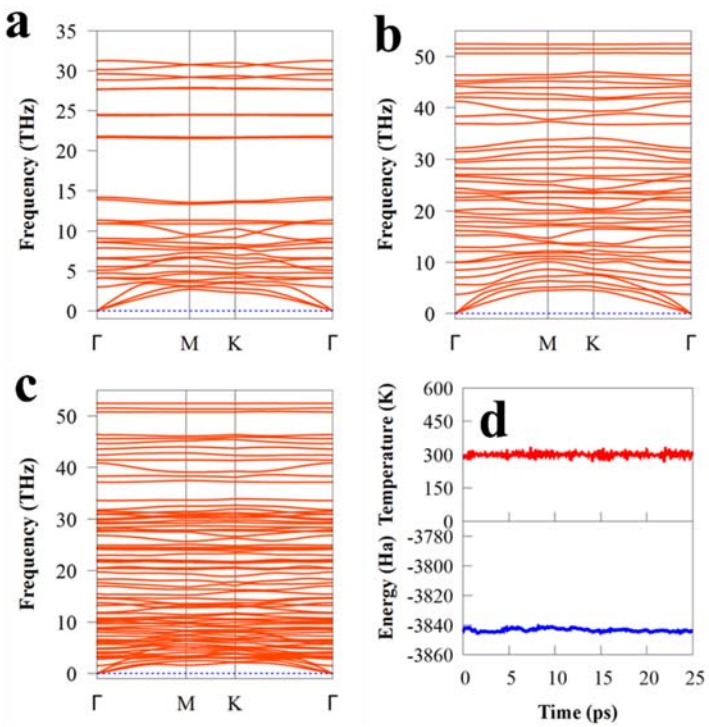

Figure S5. The phonon dispersion curves: (a) MBO, (b) dCN, (c) MBOdCN heterostructure, and (d) Time-dependent total energy and temperature fluctuations of the MBOdCN during the AIMD simulation at 300 K for 25 ps.

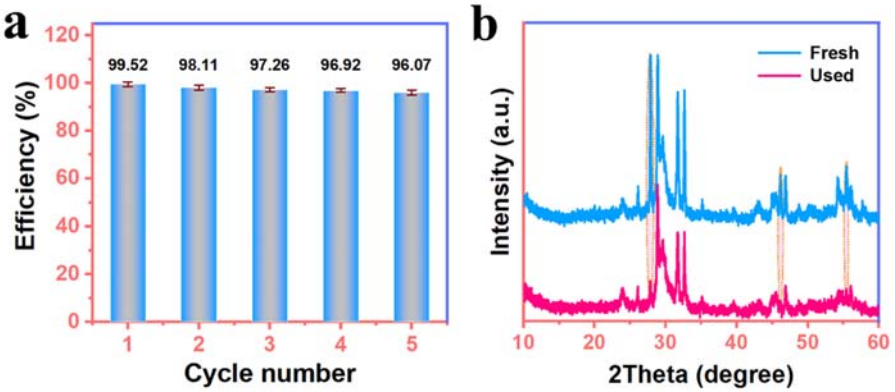

Figure S6. (a) Stability evaluation and (b) XRD pattern of fresh and used MBOdCN catalyst.

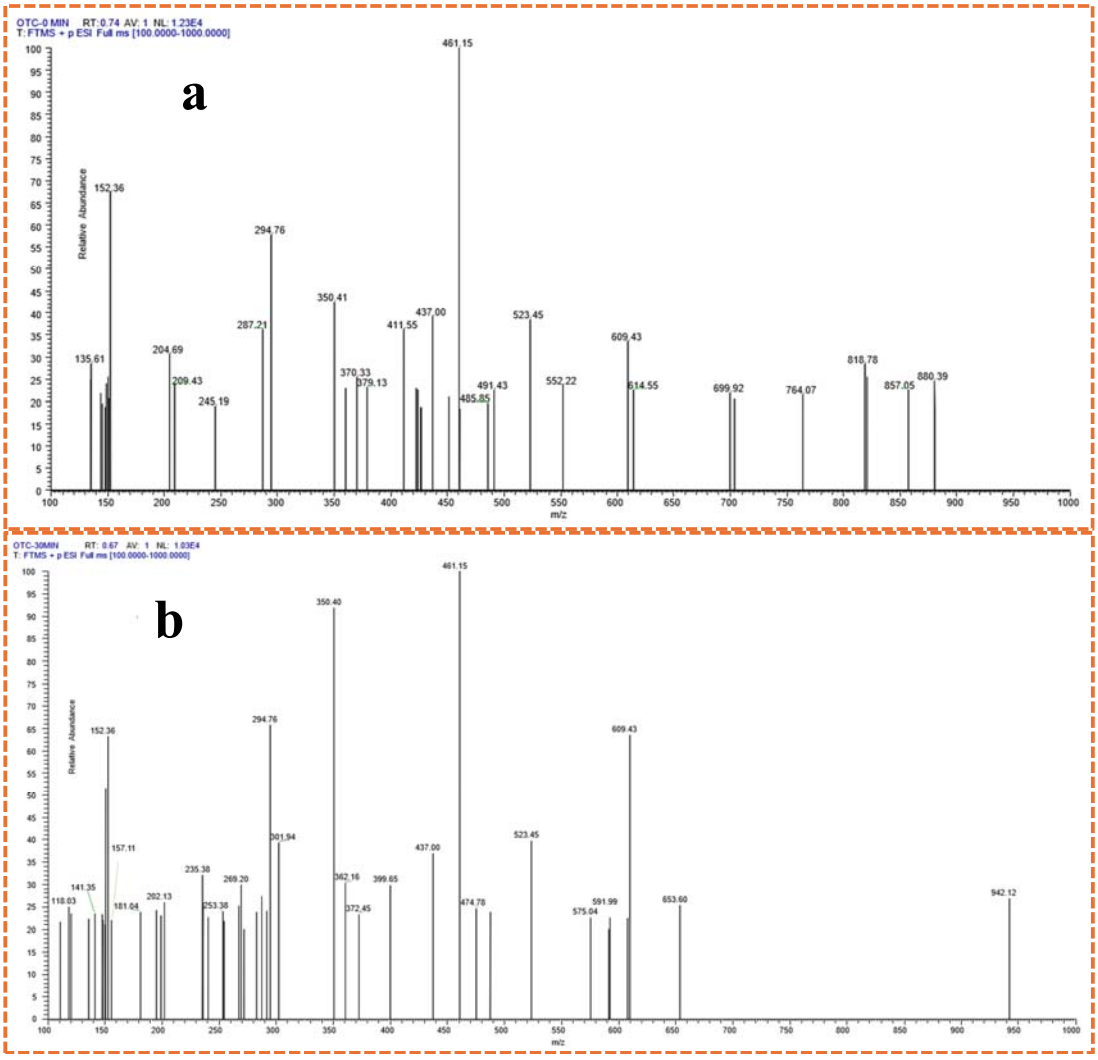

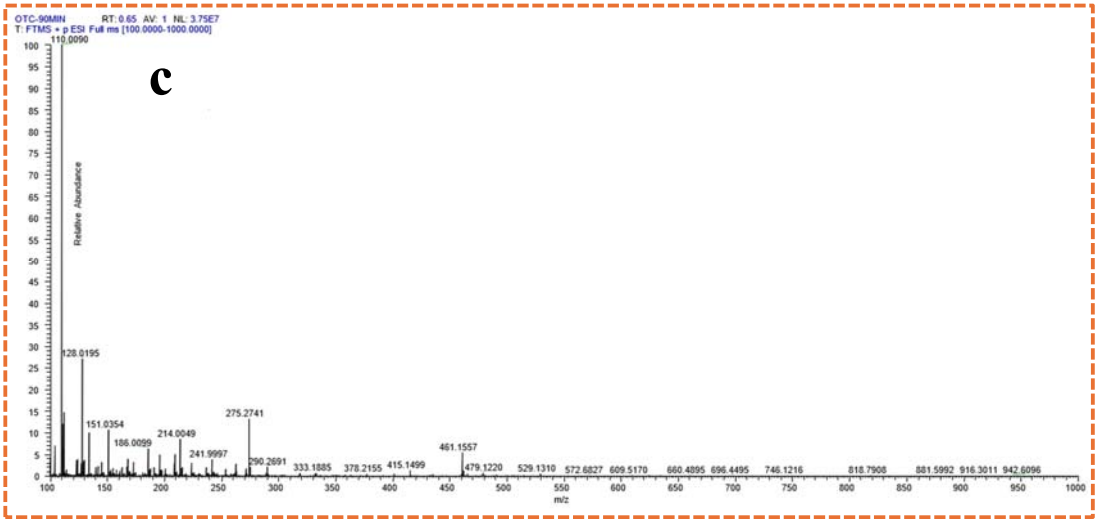

Figure S7: Mass-to-charge ratio (*m/z*) of OTC degradation by-products from LC-TOF-MS/MS at (a) 0 min, (b) 30 min, and 90 min of reaction time.

References

[1] P. J. Mafa, M. E. Malefane, A. O. Idris, D. Liu, J. Gui, B. B. Mamba, A. T. Kuvarega, *Sep Purif Technol* **2022**, *282*, 120089.

[2] X. Zhang, Y. Zhang, X. Jia, N. Zhang, R. Xia, X. Zhang, Z. Wang, M. Yu, *Sep Purif Technol* **2021**, *268*, 118691.

[3] X. Zhang, S. Chen, H. Luo, Z. Tang, E. Liu, Z. Qin, K. Xu, *Sep Purif Technol* **2023**, *305*, 122439.

[4] K. Saravanakumar, V. Maheskumar, Y. Yea, Y. Yoon, V. Muthuraj, C. M. Park, *Compos B Eng* **2022**, *234*, 109726.

[5] A. Morales-García, A. L. Soares, E. C. Dos Santos, H. A. De Abreu, H. A. Duarte, *Journal of Physical Chemistry A* **2014**, *118*, 5823.

[6] R. Zhang, Y. Zhang, X. Wei, T. Guo, J. Fan, L. Ni, Y. Weng, Z. Zha, J. Liu, Y. Tian, T. Li, L. Duan, *Appl Surf Sci* **2020**, *528*, 146782.

[7] X. Dong, L. Xu, J. Ma, Y. Li, Z. Yin, D. Chen, Q. Wang, J. Han, J. Qiu, Z. Yang, Z. Song, *Chemical Engineering Journal* **2023**, *459*, 141557.

[8] M. Cai, Y. Liu, K. Dong, C. Wang, S. Li, *J Colloid Interface Sci* **2023**, *629*, 276.

[9] P. J. Mafa, M. E. Malefane, F. Opoku, A. Sacko, A. O. Oladipo, S. L. Lebelo, D. Liu, J. Gui, B. B. Mamba, A. T. Kuvarega, *J Clean Prod* **2023**, *429*, 139519.

[10] X. Chen, F. Tian, C. Persson, W. Duan, N. X. Chen, *Sci Rep* **2013**, *3*, 3046.